The influence of the plasma-nitriding temperature on the microstructure evolution and surface properties of additive-manufactured 18Ni300 maraging steel

Matjaž Godec [a,*], Francisco Ruiz-Zepeda [a,b], Bojan Podgornik [a], Črtomir Donik [a], Aleksandra Kocijan [a], Danijela A. Skobir Balantič [a]

[a] Institute of Metals and Technology, Lepi pot 11, 1000 Ljubljana, Slovenia
[b] National Institute of Chemistry, Hajdrihova 19, 1000 Ljubljana, Slovenia

ARTICLE INFO

ABSTRACT

Maraging steel grade18Ni300 produced by powder bed fusion (PBF) in its as built condition was plasma nitrided at three different temperatures. The aim of the work was to investigate the impact of the nitriding temperature on the microstructural changes as well as on the surface properties such as hardness, wear and corrosion resistance. The microstructural features in the bulk as well as in the nitride layer were investigated using electron-backscatter diffraction (EBSD), transmission electron microscopy (TEM) and X-Ray diffraction (XRD) analysis. The bulk microstructure consists of martensite with a small amount of retained austenite, the amount of which increases with a higher nitriding temperature. The nitriding process also causes the formation of precipitates and can therefore also act as an aging treatment. A specific lamellar structure occurs on the surface during the nitriding process, which in the majority of cases consists of the Fe_4N phase. The retained austenite also transforms during nitriding to the nitride phase Fe_4N. It was found that nitriding at higher temperatures leads to the formation of cracks in the nitride layer. The crack formation is related to nano and micro segregation during the LPBF. These segregations lead to austenite formation, which also takes place along the grain boundaries and transforms during nitriding to Fe_4N. Higher nitriding temperatures lead to a thicker nitride compound layer and to better wear resistance. The impact of the cracks on the static mechanical properties is negligible. However, the corrosion resistance is governed by the formation of cracks at higher nitriding temperatures.

1. Introduction

Maraging steels belong to the class of low-carbon, nickel-rich martensitic steels that exhibit a unique combination of high strength and hardness together with good toughness, ductility and weldability [1–3]. Therefore, they are applied as tool steels in the tool-and-die-making industry as well as in automotive, aerospace and military [4,5]. The martensitic microstructure responsible for the high toughness and ductility is not achieved with a high amount of carbon as in most tool steels, but by a high concentration of nickel. The ultra-high strength of maraging steels is derived from a strengthening mechanism caused by the precipitation of nanometre-sized intermetallic phases (Ni_3Ti, Fe_2Mo, NiAl) during appropriate aging heat treatments [6,7]. These particles are homogeneously distributed in the low-carbon, soft martensitic microstructure. In addition to the precipitation, austenite reversion can

also take place during aging [8,9]. The amount of reverted austenite depends on the alloy composition and is formed around a region of retained austenite, which remains in the microstructure after quenching. Austenite reversion is important for the magnetic properties of the steel, while retained austenite, on the other hand, deteriorates the mechanical properties [9].

Maraging steels possess some disadvantages in terms of surface mechanical properties, especially poor wear and corrosion resistance [10–12], especially in comparison to other tool steels or stainless steels. Therefore, a thermochemical treatment such as plasma nitriding is an effective and widely used method to improve the surface mechanical properties of conventionally manufactured maraging steel. Due to the similar process parameters of the plasma nitriding and aging heat treatment (temperatures between 430 and 520 °C, times of 1–6 h), it is also possible to combine both processes in a unique single step,

important especially in terms of cost and time saving [13,14].

Due to their characteristics, maraging steels, especially 18Ni300 (also known as C300 grade maraging steel), have gained a lot of attention in the field of additive manufacturing (AM) technologies, in particular directed energy deposition (DED) and powder bed fusion (PBF). There are two main reasons for it being well suited to PBF [8]: (i) the rapid solidification and high cooling rate of the PBF process enable the formation of the martensite matrix and (ii) the use of maraging steel for aerospace and tooling components, where the fabrication of complex geometries and small quantities are required. These are demands that can easily be achieved with PBF.

High cooling rates and rapid solidification during PBF generate a very fine, cellular structure, consisting mainly of martensite with no precipitates [8]. Thus PBF-processed maraging steels have, in their as built state, high yield and tensile strengths and hardness, but low ductility and toughness [15–17]. For most applications of PBF-processed maraging parts is therefore necessary to guarantee a similar combination of these properties as they are obtained by conventional processing. A number of studies have already confirmed that PBF-processed maraging steel has to be heat-treated after the PBF as well to obtain the desired mechanical properties. A solution treatment, an aging treatment or a combination of both are the heat-treatment processes that can improve the microstructure and mechanical properties of the parts from PBF. However, the heat-treatment processes for PBF-processed maraging steel can differ from the conventional ones due to the difference in the microstructure of the conventional (cast or wrought) and PBF-produced maraging steel [18]. Bai et al. [19] carried out a comprehensive numbers of heat-treatment experiments (including solution treatment, direct aging treatment and solution+aging treatment) at different temperatures and for different times to investigate their influence on microstructure evolution and mechanical properties (microhardness, tensile properties, toughness). Several authors [4,20–23] focused on the importance of a proper aging treatment for improving the mechanical performance of PBF-processed maraging steels by inducing the precipitation of different kinds of precipitates. Besides the precipitation hardening, an austenite reversion is another important phenomenon occurring during aging, which significantly influences the microstructure and the mechanical properties of PBF-processed parts and was reported by Conde et al. [6] and Jaegle et al. [8].

Maraging steels are materials for severe environments like the tooling and mould industries, where superior wear and corrosion resistance are required [24]. Thermochemical treatments such as plasma nitriding can therefore represent a promising step forward for improving the surface properties of PBF-produced maraging steels. Nevertheless, there are only a few studies reporting the use of plasma nitriding and its beneficial effect for PBF [12,25,26]. Godec et al. [26] performed a comparison of wear and corrosion properties after the plasma nitriding of PBF-processed and conventionally manufactured 18Ni300 maraging steel. Hong et al. [12] investigated the characteristics of plasma nitriding in combination with various heat treatments for 18Ni300 maraging steel. On the one hand, both investigations proved an improvement of the surface properties after plasma nitriding. On the other hand, it became obvious that the plasma nitriding of PBF-processed materials remains ambiguous, especially in terms of temperature-dependent nitride-layer formation as well as in the precipitation behaviour in the nitride layer and in the bulk. It therefore needs further investigation.

In this work, as built PBF-18Ni300 steel was plasma nitrided at three different temperatures to investigate the influence of the nitriding temperature on the formation and the thickness of the nitride layer. One of the main aims of this work was to investigate the tribological and corrosion properties, such as wear and corrosion resistance which are among the most important surface properties, and their dependence on the plasma nitriding temperature. The second aim was to understand the microstructure evolution in the nitride layer where cracks were formed during higher temperature nitriding and to propose the explanation for

cracks formation. The last but not the least aim was to understand microstructure changes in the bulk during nitriding process.

2. Materials and methods

2.1. Material preparation

Maraging steel grade 18Ni300 with the chemical composition (wt%) of 17.8% Ni, 8.8% Co, 5.0% Mo, 0.80% Ti, 0.04% Mn, $\leq$ 0.1% Cr, $\leq$ 0.10% Si, $\leq$ 0.003% C, $\leq$ 0.001% S and the balance of Fe, was produced by an industrial powder-bed fusion system EOS EOSINT M280. The feedstock for the PBF process consists of gas-atomized powder particles with sizes between 15 and 45 μm. Commercial PBF process parameters (a laser power of 285 W, a laser speed of 960 mm/s, distance between the laser paths 0.11 mm, hatching in x and y, alternating and rotating) were used to build the samples of dimensions of $30 \times 30 \times 30$ mm³. An atmosphere of 99.5% purity nitrogen was used during the additive manufacturing.

Prior to the plasma nitriding, the as built samples' surfaces were mechanically prepared by grinding and finally polished down to Sa = 0.18 μm with a suspension of 1-μm diamond to remove any surface deformations. Afterwards, the samples were plasma nitrided in a gas atmosphere of 75 vol% H_2 and 25 vol% N_2 at three nitriding temperatures: N1 = 440 °C, N2 = 480 °C and N3 = 520 °C for 6 h, resulting in somewhat increased surface roughness of $Sa_{N1} = 0.25 \pm 0.02$ μm, $Sa_{N2} = 0.23 \pm 0.01$ μm and $Sa_{N3} = 0.23 \pm 0.02$ μm, respectively. The plasma nitriding was conducted in a Metaplas Ionon HZIW 600/1000 cold-wall reactor. Table 1 presents the labels and the conditions of investigated samples.

2.2. Microstructural characterization

The microstructural characterization was performed on cross-sections, prepared by standard metallographic techniques (mounting in conductive Bakelite resin, grinding, polishing and final etching in Nital (2% nitric acid in ethyl alcohol). The microstructure was observed using the light microscope Nikon Microphot FXA with installed digital camera Olympus DP73. A field-emission scanning electron microscope (FE-SEM), ZEISS CrossBeam 550 FIBSEM, equipped with an EDAX Hikari Super EBSD camera, was used for the detailed microstructural characterization with EDAX TEAM software. Secondary-electron imaging (SEI), energy-dispersive spectroscopy (EDS) and electron-backscatter diffraction (EBSD) were carried out on FE-SEM. SE images and EDS analyses were performed using a 15-kV accelerating voltage and a 2.0–5.0 nA probe current, while the EBSD measurements were carried on 70°-tilted samples with a 7.0-nA probe current for the phase composition.

(Scanning) Transmission electron microscopy ((S)TEM) analysis was performed in a Cs-corrected JEOL ARM 200 CF equipped with SSD JEOL EDS spectrometer and Gatan dual electron energy loss spectroscopy (EELS) Quantum spectrum-imaging filter.

A Panalyitical X'PERT Pro PW 3040/60 goniometer with Bragg-Brentano geometry (XRD) was also used for the phase composition. The samples were analysed using a 2θ goniometer 15°–90° with a step size of 0.002° and a scan step time of 100 s at each step. Cu with (K_α = 0.154 nm) anode was used with a current of 40 mA and a potential of 45 kV.

Table 1
Labels and the sample conditions.

Label	Sample description
AM	Additive manufactured 18Ni300 as-built
AM+N1	Additive manufactured 18Ni300 as-built and nitrided at 440 °C
AM+N2	Additive manufactured 18Ni300 as-built and nitrided at 480 °C
AM+N3	Additive manufactured 18Ni300 as-built and nitrided at 520 °C

2.3. Wear tests and hardness measurements

The tribological behaviour (wear volume and coefficient of friction) of the as built and nitrided samples was analysed by reciprocating dry-sliding wear tests on a tribometer with the ball-on-disc contact geometry. To simulate sliding wear and concentrate the wear on the maraging steel disc, a harder Al_2O_3 ball with a diameter of 20 mm was selected as the oscillating counter-body. For each sample, three parallel tests at room temperature were carried out. The following test parameters were used: normal load of 20 N, corresponding to the nominal contact pressure of 800 MPa, amplitude of 4 mm and frequency of 15 Hz, resulting in an average sliding speed of 0.12 m/s, a testing time of 1000 s and a total sliding distance of 120 m.

A high-resolution 3D confocal focus variation microscope (Alicona InfiniteFocus G4 3D) was used to analyse the wear tracks and to measure the wear volumes. The coefficient of friction was measured continuously as a function of the testing time and the average steady-state value was calculated.

The bulk hardness and the surface hardness of the nitrided layers were measured with an Instron B2000 Rockwell hardness tester (HRC). The depth profiles of the nitrided layers were measured with an Instron Tukon 2100 B Vickers hardness tester (HV0.01).

2.4. Electrochemical measurements

Potentiodynamic measurements were performed in a 3.5% NaCl solution at room temperature. The electrochemical cell consisted of the investigated sample as a working electrode, a reference electrode (a saturated calomel electrode – SCE, 0.242 V vs. SHE) and a platinum-mesh counter electrode. The measurements were performed using a BioLogic® SP-300 Model Potentiostat/Galvanostat/FRA and EC-Lab® V11.27 software. Prior to the experiment, the samples were stabilised at the open-circuit potential for 1 h and the measurements were repeated three times to obtain statistically relevant results.

3. Results and discussion

3.1. Microstructures

The samples of PBF-manufactured maraging steel were plasma nitrided in their as built condition. The plasma nitriding was performed at three temperatures (N1 = 440 °C, N2 = 480 °C, N3 = 520 °C) for 6 h. Nitriding primarily caused the formation of a nitride layer due to N penetration as well as to changes of bulk microstructure due to heating of the samples during the nitriding. As the nitriding temperatures are similar to the aging temperatures, nitriding can also act as the aging. That means that both processes are carried out simultaneously.

According to the Thermo-Calc Software (version Thermo-Calc 2021b, database TCFE11) calculation (Fig. 1) the microstructure of maraging steel consists of the bcc (martensite) and a small amount of fcc phase (austenite). The amount of austenite phase in the equilibrium increases with the temperature and is 26% to 35% in the temperature range from 440 °C to 520 °C. Therefore, it is expected that nitriding will increase the amount of austenite phase and will be higher at higher nitriding temperatures. In the temperature range of nitriding, precipitates are also present: ~10% of Fe_2Mo and ~ 4% $Ni_3(Ti, Mo)$ [27,28].

In our previous work, about 3% of austenite was detected in the AM sample [26] with EBSD measurements. Fig. 2 shows microstructures with EBSD IPF Z combined with phase maps of the bulk of maraging steel after being subjected to nitriding at three different temperatures. EBSD maps (Fig. 2a-c) show a typical AM microstructure with columnar grains of lath martensite with some amount of austenite. After the PBF the microstructure consists of martensite and a small amount of retained austenite [26]. Due to the higher stability of the austenite at higher temperatures, the amount of austenite increases and consists of retained
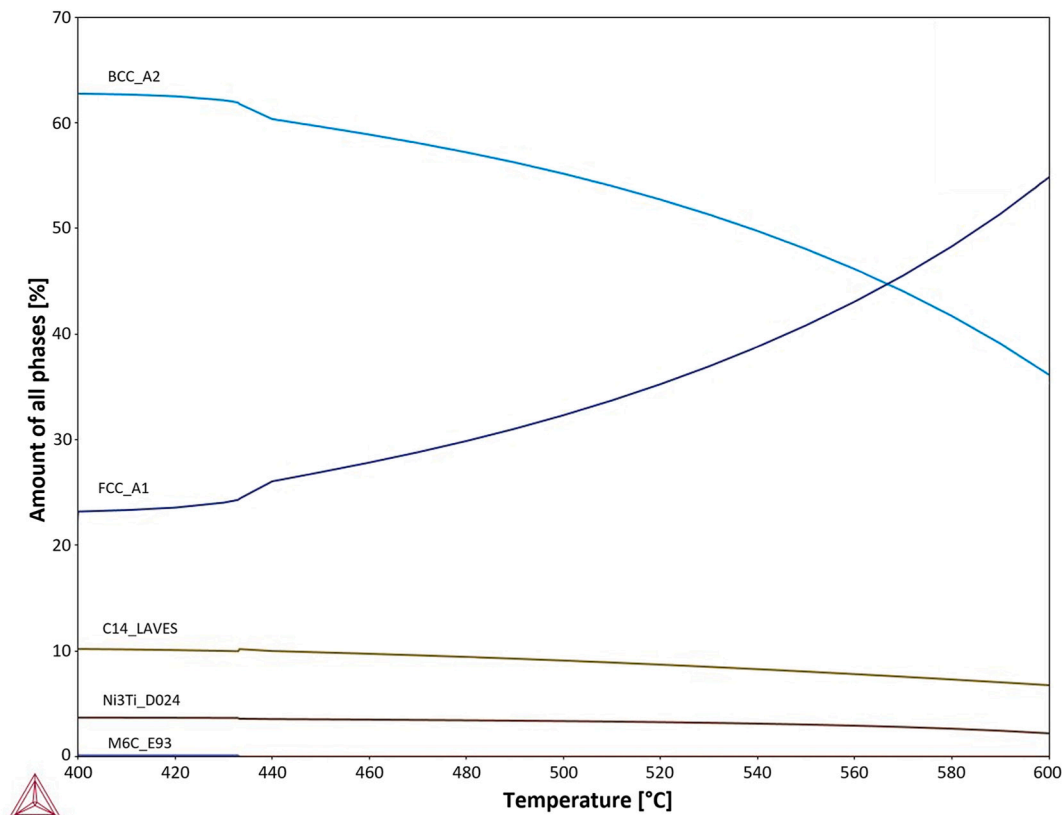

Fig. 1. ThermoCalc thermodynamic calculation for thermodynamically stable phases in 18Ni300 for the temperature range of nitriding.
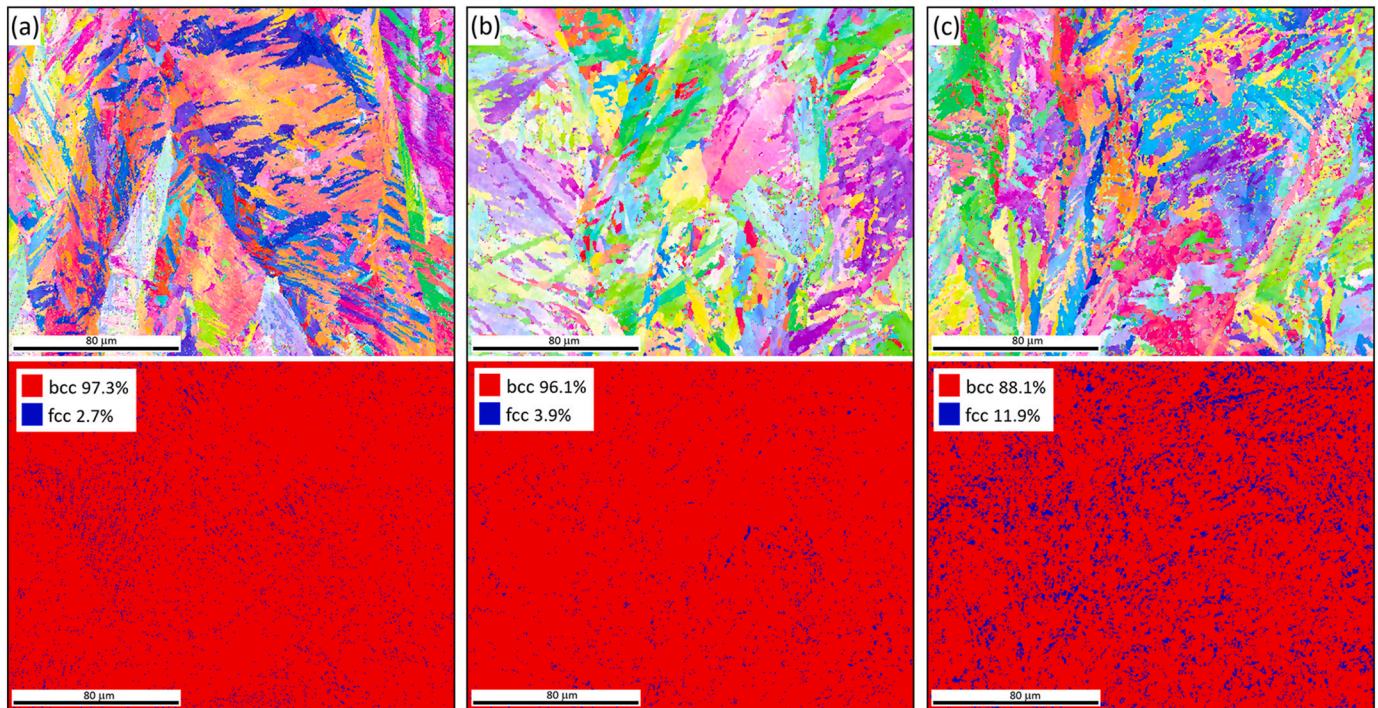
Fig. 2. EBSD IPF Z and phase maps in the BD direction of samples: (a) AM+N1, (b) AM+N2, (c) AM+N3.

and reverted austenite. The amount of reverted austenite does not change much at the nitriding temperatures of 440 °C and 480 °C, and is 2.7%, 3.9%, respectively (Fig. 2d-e). A higher nitriding temperature (520 °C) leads to a significant increase of austenite, i.e., 11.9% (Fig. 2f). The morphology of the martensite remains almost the same during the nitriding process at all three temperatures.

The bulk microstructure at the nitriding temperature of 520 °C was also investigated by TEM to reveal the microstructure and particularly the precipitates (Fig. 3). The selection of the highest nitriding temperature is based on the following: a higher amount of austenite, the formation of cracks and a larger amount and size of precipitates. Fig. 3a shows a STEM ADF image taken at a smaller magnification exhibiting many precipitates, including some grey areas and also some darker spherical particles. Fig. 3b is an enlarged area from the yellow square marked in Fig. 3a and showing one larger spherical particle, some smaller precipitates in a quasi-spherical and needle-like shape. Fig. 3c corresponds to one of the grey areas oriented in the zone axis to analyse the atomic structure, which is shown in Fig. 3d. The corresponding fast Fourier transform (FFT) shown in Fig. 3e revealed that the distances identified from the lattice planes matched the austenite phase, which was also observed by EBSD (Fig. 2c). From the EDS maps (Fig. 3f) it is evident that the large particle has a Ti-Mo-N ring and the core of Al-Ti-O-N. These kinds of particles are inclusions formed during the PBF process where the local temperatures are high enough to melt the powder particles as well as the (non)-metallic inclusions inside the powder particles. The small, quasi-spherical precipitates of size 20–30 nm are (Mo, Fe)-rich, while the small needle-like precipitates of length 30–50 nm and up to 10 nm thick are (Ni, Ti)-rich and Co depleted (an example is marked with an arrow in Fig. 3f). Based on literature data the observed precipitates are $Ni_3(Ti, Mo)$, Fe_2Mo [27,28] and at longer aging times Fe_7Mo_6 [29–31]. The dashed white line in Fig. 3a shows the cellular structure formed during AM [32]. There are a higher amount of dislocations on cell borders with Ni, Ti, and Mo positive segregation [18]. During nitriding, this area (cell border) starts transforming to the austenite phase because these areas contain more γ-stabilizing elements. From the EDS maps it is evident that this area is rich in Ni and Mo and fewer precipitates are formed due to the higher solubility in the fcc

phase. From the literature [33], it is known that some nano oxides are formed on cell borders in stainless steel; therefore, it is expected that titanium aluminides are formed in maraging steel during AM (observed as black spots in Fig. 3a) and located at the cell borders.

The microstructure (cross-sections) of the maraging steel samples is presented in Fig. 4a-c as light micrographs and in Fig. 4d-f as SE images. The sample geometry with the indicated building direction (z-axis), position of nitride layer and the cross-section for the microstructural characterization are illustrated in the inset of Fig. 4a. The bulk microstructure and the nitride layer on the top of the samples are seen on all images.

A typical AM cellular solidification structure with visible melt pools (Fig. 4) is observed on all samples. Some of the microstructural features were already described in a previous publication [26]. The nitride layers consist of a very thin compound layer on the top of the sample and the diffusion layer beneath. The thickness of the nitride layer is temperature dependent and increases with a higher temperature. The compound layer is very indistinct, almost invisible for samples AM+N1 (Fig. 4a) and with an estimated thickness of ~2 μm and ~5 μm for the samples AM+N2 (Fig. 4b) and AM+N3 (Fig. 4c), respectively. The diffusion layer beneath the compound layer is seen as a dark area. An exact estimation of its depth is not possible due to the etching effect. The SE images (Fig. 4d-f) show some interesting features. The nitride layers exhibit a unique microstructure (inset in Fig. 4f) resulting from the combination of additive manufacturing plus nitriding, described also by Hong et al. [12]. It can be described as an interlaced lamellar structure consisting of coarse and fine lamellas. Such a microstructure is observed at all nitriding temperatures, but it is more pronounced at higher temperatures and is not observed after the nitriding of conventionally manufactured maraging steel.

The nitriding at higher temperatures (N2 and N3) causes the formation of cracks (Fig. 4e and f). In sample AM+N1 no cracks were observed, even for a detailed observation of a larger area. It is well known that the AM process due to rapid solidification causes internal stresses [34,35], which can lead, depending on AM parameters and materials, to the formation of cracks. Usually, the material is post-process heat treated to release the internal stresses and to avoid
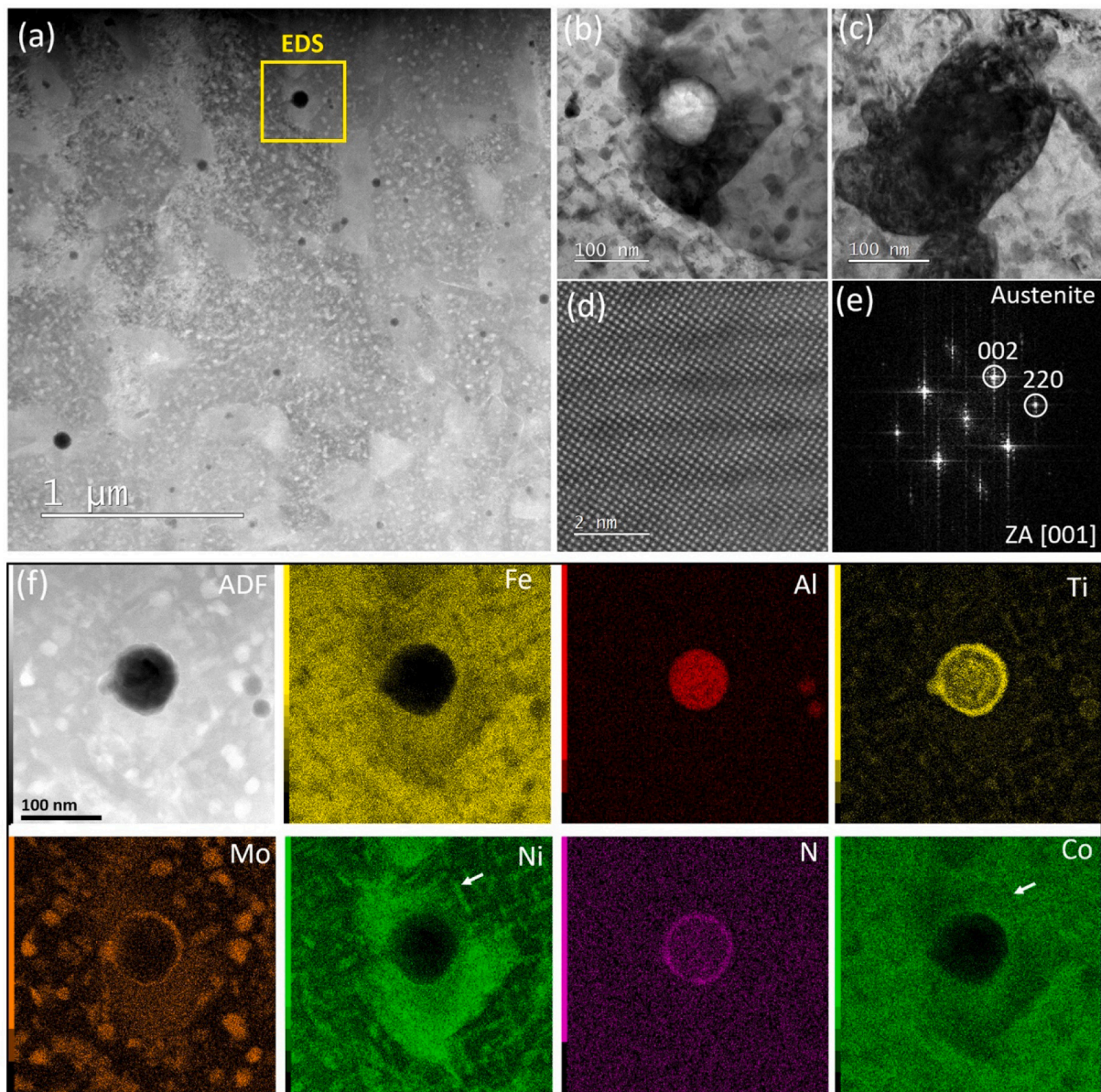
Fig. 3. (a) STEM ADF image taken from the bulk area of sample AM+N3, (b) STEM BF image corresponding to the EDS mapping region, (c) a grey area in zone axis, (d) STEM ADF high resolution image from the grey area, (e) corresponding FFT showing an austenite structure. (f) ADF and EDS mapping of Fe Kα, Al Kα, Ti Kα, Mo Lα, Ni Kα, N Kα and Co Kα.

cracking. The investigated as built samples were crack-free. The nitriding was performed without prior heat treatment; therefore, it is assumed that the samples contain internal stresses. Higher nitriding temperatures cause more cracks, mostly along grain boundaries. The combination of internal stresses and N penetration is the most likely explanation for the origin of the cracks' formation. On the one hand, the crystal structure is enlarged due to interstitial N incorporation, while on the other hand, the excess of N causes the formation of th eFe_4N phase, which has a larger volume.

The EDS depth profiles of the elements through the nitride layer were measured to obtain information about the penetration depth of the nitrogen and the distribution of other alloying elements and to compare the depth of diffusion zone for all three nitriding temperatures (Fig. 5). The dashed lines in all three images represent the SEI darker area of diffusion layers, which corelate with the depth of nitrogen and range from 55 μm in the sample AM +N1, to 90 μm in sample AM+N2 and 125 μm in sample AM+N3. The EDS line profile for Ni is smooth in samples AM+N1 and AM+N2, while in the sample AM+N3 the Ni line is more

serrated, which can be explained by the larger amount of austenite phase. Ni solubility is higher in the austenite phase than in the martensite phase since Ni is the γ-stabilizing alloying element. A similar phenomenon occurs with N, which is also a γ-stabilizing alloying element. Therefore, the measurements show a higher concentration of N in the austenite as well. The maximum EDS line peaks of Ni and N corelate well with the minimum EDS peaks of Fe.

The microstructure of the nitride layer in sample AM+N3 investigated with TEM is presented in Fig. 6. The FIB-thinned TEM specimen was extracted from the region set about 4 μm from the surface, close to the boundary between the compound and diffusion layers, albeit still inside the compound layer. The lamellar structure observed as dark and bright lamellas (BL and DL) in the STEM ADF image from Fig. 6a also contains small dark spherical inclusions of similar composition to the ones already described for the bulk (Fig. 3f). At the cellular borders, similar morphologies of the structures (phase X) are observed as in the bulk, which were detected as austenite. An EDS analysis (Fig. 6b) was performed in the region marked by a yellow square in Fig. 6a. The
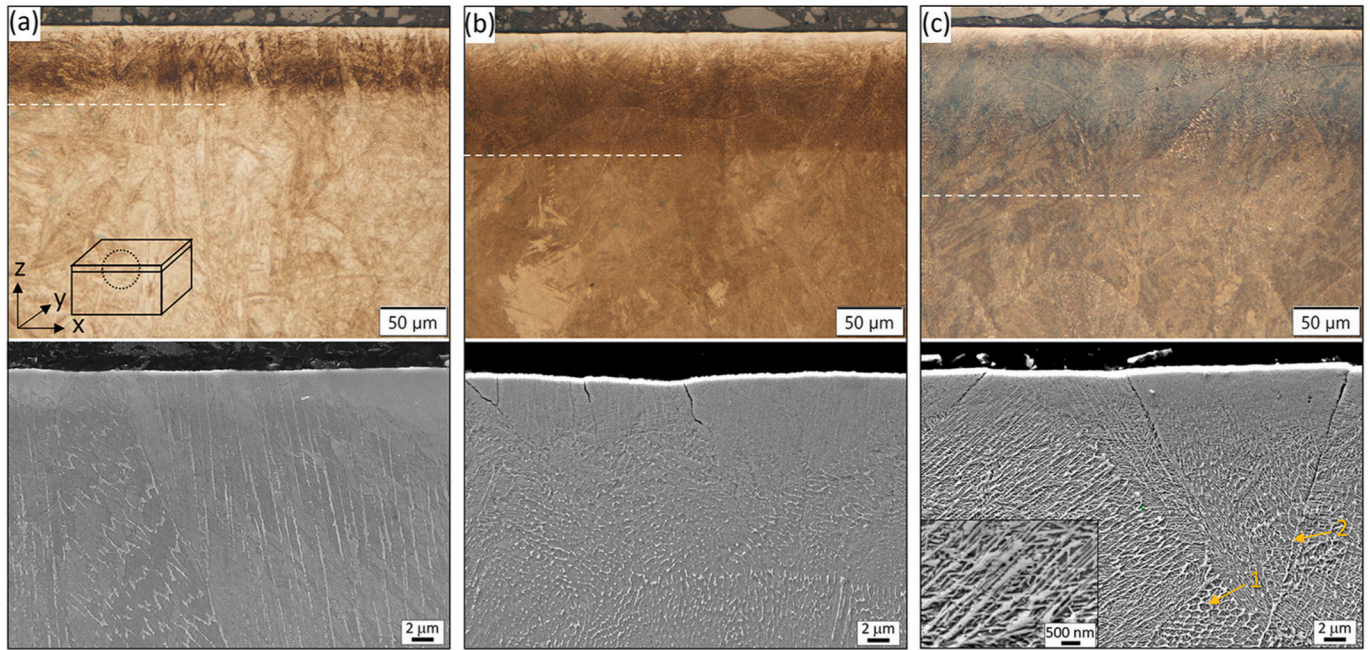
Fig. 4. Light micrographs and SE images of samples: (a) AM+N1, (b) AM+N2, (c) AM+N3. The white dashed lines represent the thickness of the diffusion layer. The inset in (a) shows the sample geometry and the inset in (c) shows the typical lamellar structure of the nitride layer.
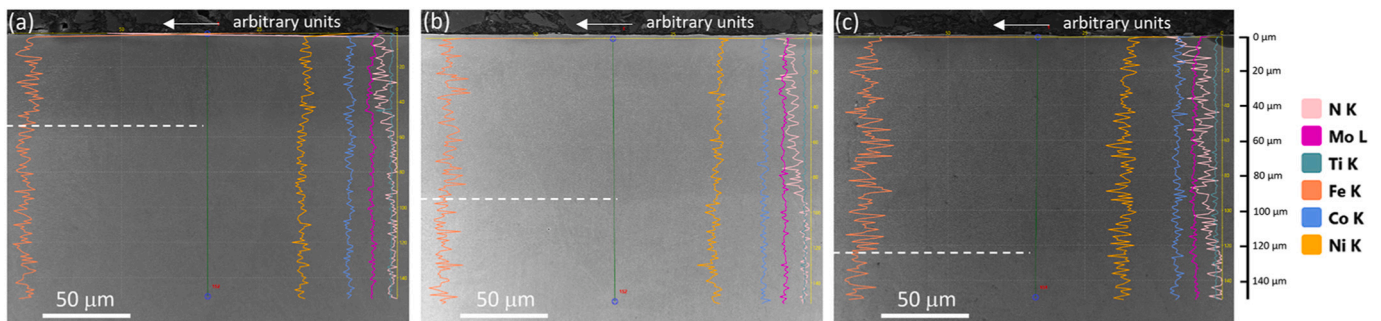

Fig. 5. EDS line profile on SE images of (a) AM+N1, (b) AM+N2 and (c) AM+N3. The diffusion zone is marked with a dashed white line.

elemental distribution of different phases shows that the bright lamellas have an excess of Co, while the dark lamellas correspond to Co depletion. Phase X is N-rich, but also contains Ti and Mo, while Ni is concentrated on the border. An EELS analysis was performed in the lamellar structure in order to verify the presence of N. As can be seen from Fig. 6c, the regions containing N correspond to the dark lamellas, while the regions that are N depleted but contain Co correlate well with bright lamellas from the ADF image. Fig. 6d and Fig. 6e are high-resolution ADF images with the corresponding fast Fourier transform (FFT) indicating plane distances identified as martensite and Fe_4N phase from the bright and dark lamellas, respectively. Fig. 6f and Fig.6g are TEM images and diffraction patterns from phase X and the matrix. The structures identified in phase X correspond to overlapping TiN and Fe_4N. Based on these observations, it is evident that retained austenite transforms during nitriding to a nitride phase (Fe_4N). The matrix consists of bright and dark lamellas, whereas the dark lamellas transform to Fe_4N, the bright lamellas most probably remain as martensite or partly transform to reverted austenite, as discussed in detail in the XRD results.

Compared to the bulk structure in the same sample there are no precipitates. The formation of the compound layer occurs typically by growth due to the penetration of nitrogen during the nitriding process and therefore it is expected that the compound layer is free of precipitates.

The XRD analyses were performed for the phase confirmation formed during PBF process as well as those formed during nitriding (in the nitride layer and in the bulk). Therefore, XRD spectra were measured on the AM sample, on the surface of the nitride layer of all the nitride samples (AM+N1 surf., AM+N2 surf., AM+N3 surf.), as well as in the bulk of the nitride samples (AM+N1 bulk, AM+N2 bulk, AM+N3 bulk) where the nitride layer was removed by grinding and polishing (Fig. 7). The thickness of the removed surface layer was over 500 µm in order to reach the bulk area. The AM sample's spectra reveal martensitic microstructure with a small amount of retained austenite, which correlates with our previous findings [26]. The spectra (AM+N1 bulk, AM+N2 bulk and AM+N3 bulk) show that the amount of retained austenite increases with a higher nitriding temperature, proved also by the EBSD measurements in Fig. 2. In the XRD spectra of the samples' surface, the formation of nitride (Fe_4N) is observed with the higher temperature increment. The peaks of Fe_4N are broadened due to the nano/sized nitrides in the structure [36]. The nitride peaks become narrower and higher with the nitriding temperature due to the growth of nitrides. The penetration of nitrogen into the fcc structure shifts the peaks of martensite to lower 2θ degrees due to crystal lattice expansion (larger d values) and, at the same time, broadened peaks [37]. It seems that some retained austenite is formed during nitriding at the highest temperature. The peak is very broadened and weak. The TEM results
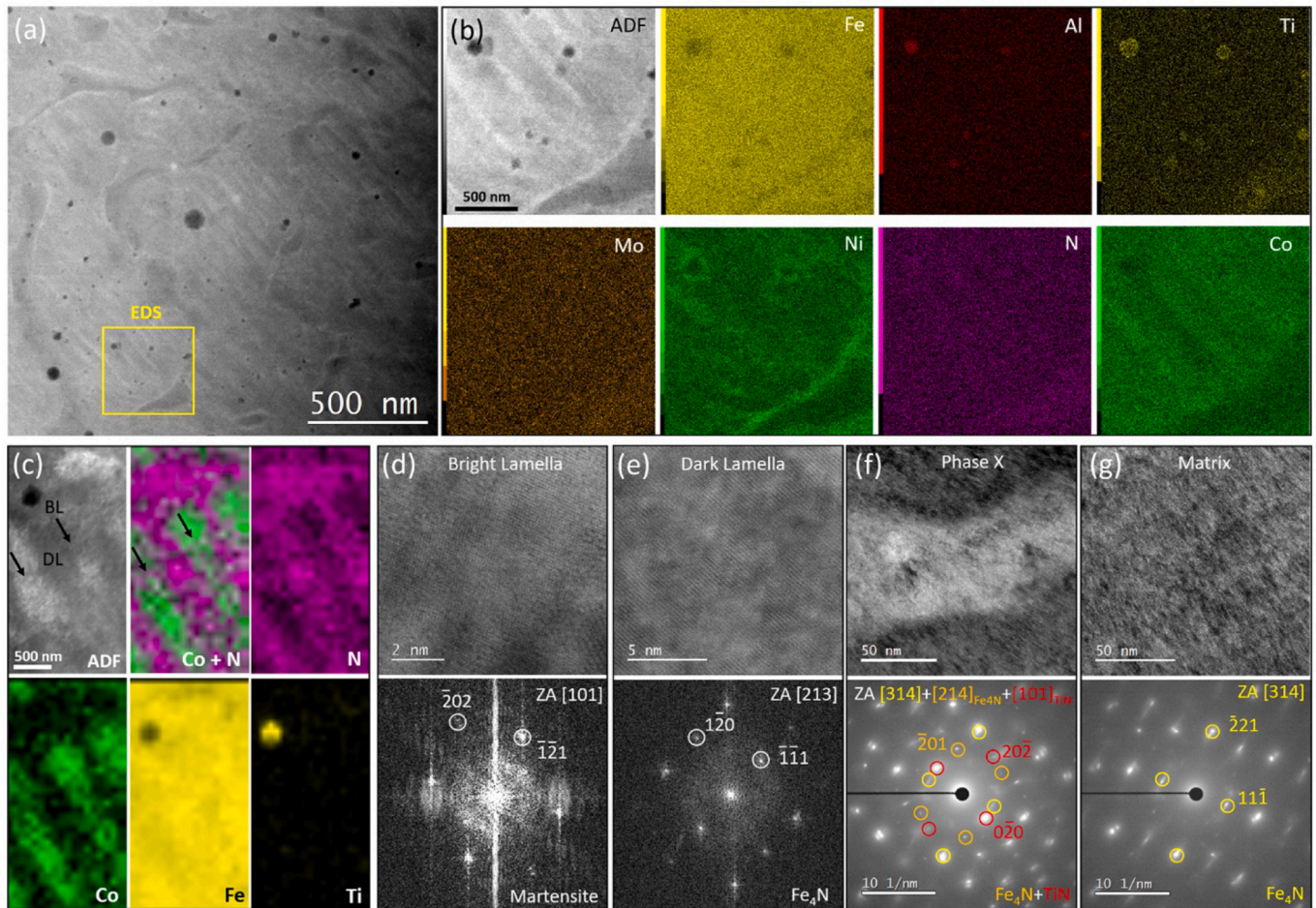
Fig. 6. (a) STEM ADF image in the compound nitride layer of sample AM+N3, (b) STEM ADF from the corresponding EDS mapping region and signals from Fe Kα, Al Kα, Ti Kα, Mo Lα, Ni Kα, N Kα and Co Kα, (c) ADF and EELS mapping corresponding Co + N, N, Co, Fe and Ti distribution, (d) High-resolution ADF image and FFT from the bright lamella region displaying a martensite structure, (e) High-resolution ADF image and FFT from the dark lamella region showing a Fe₄N structure, (f) TEM image and diffraction pattern from the phase X morphology region, the identified structure corresponds to overlapping of TiN and Fe₄N, (g) TEM image and diffraction pattern from the matrix identified as Fe₄N.

indicate the possibility of TiN formation in the nitride layer, but the amount is very small due to there being only 0.8% of Ti in the chemical composition. However, the XRD detection of the TiN is below the detection limit; therefore, no TiN peaks are present.

Based on the SEM, TEM and XRD results the explanation of the crack formation in the nitride layer can be possible. Under the same nitriding conditions, no cracks were observed in the conventional material [26]. Therefore, it is the PBF process that creates internal stresses in the material and leads to crack formation. From Fig. 4e-f it is evident that most of the cracks start at the surface at the grain boundaries and propagate along the grain boundaries. A typical feature of the AM process is to form a cellular structure with nanosegregation. Jaegle et al. [18] also reported Ni, Mo and Ti segregation along the cellular borders in directed energy deposition. The results of this paper show the segregation of the same elements during the PBF process, which is in some way expected, but the cellular structure after PBF is much finer. The cellular structure is clearly visible in the etched cross-section shown in Fig. 4f, marked by arrow 1. The cellular boundaries have the segregation of Ni, Mo and Ti and are therefore less etched, which is seen as a set of cells. Similar, less-etched areas are visible along the dendrite sub-grains, the dendrite grains [38] as well as the grain boundaries. The segregation along the grain boundaries is evident in Fig. 4f, marked by arrow 2, where the crack and its propagation along the grain boundary is seen as well. The negative formation enthalpy for TiN is larger than for Fe₄N [39] and, therefore, TiN is formed primarily on the segregation areas. The

formation of TiN causes a larger expansion of the volume than the formation of Fe₄N. This is one of the possible reasons for the crack formation together with the internal stresses in the PBF-processed material. At the nitriding temperature of 440 °C no cracks were observed. Therefore, it is assumed that the main reason is the thinner compound layer, the slower diffusion rate and fewer larger nitrides that are formed.

3.2. Hardness and wear resistance

Hardness measurements are one of the important assessments of surface properties for the nitride layers. The depth profiles through the nitride layer in cross-section were measured as well as the hardness on the nitride layer's surface (Fig. 8). The surface of the nitride layer is rough because the compound layer grows during nitriding, therefore a measurement of the Vickers hardness with low loads is not suitable. The hardness from the top was measured by Rockwell, where the hardness of the bulk also contributes to the result due to a very thin nitride layer. The HRC values are 54.3, 54.9 and 51.3 for the samples AM+N1, AM+N2 and AM+N3, respectively. It is surprising that the lowest hardness was obtained in the sample that was nitrided at the highest temperature (AM+N3) where the nitride layer is the thicker. Similar results were obtained during the Vickers depth-profile measurements. The highest hardness was obtained for the sample AM+N1. The drop of the hardness correlates with the nitriding depth. The same correlation of the hardness drop can also be seen for samples AM+N2 and AM+N3.
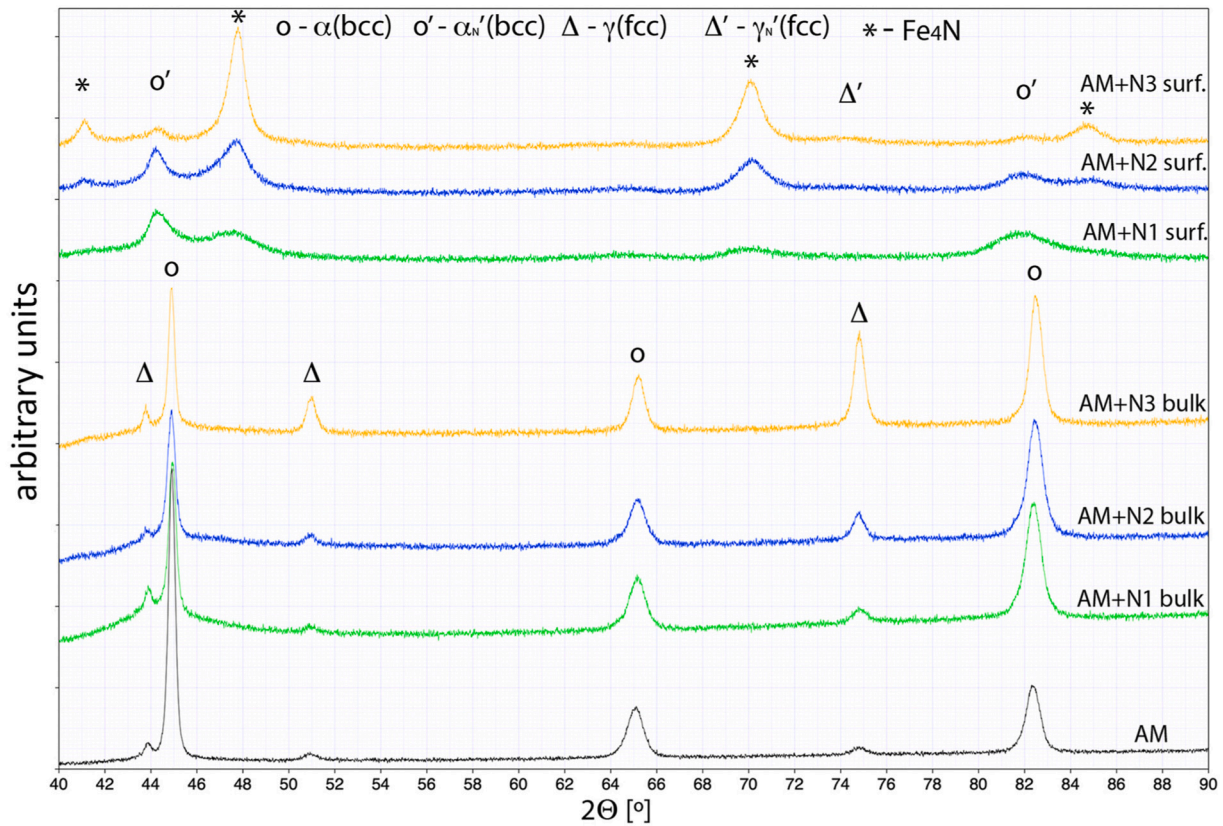
Fig. 7. XRD spectra of as built PBF sample, and nitrided samples in the bulk and on the surface.
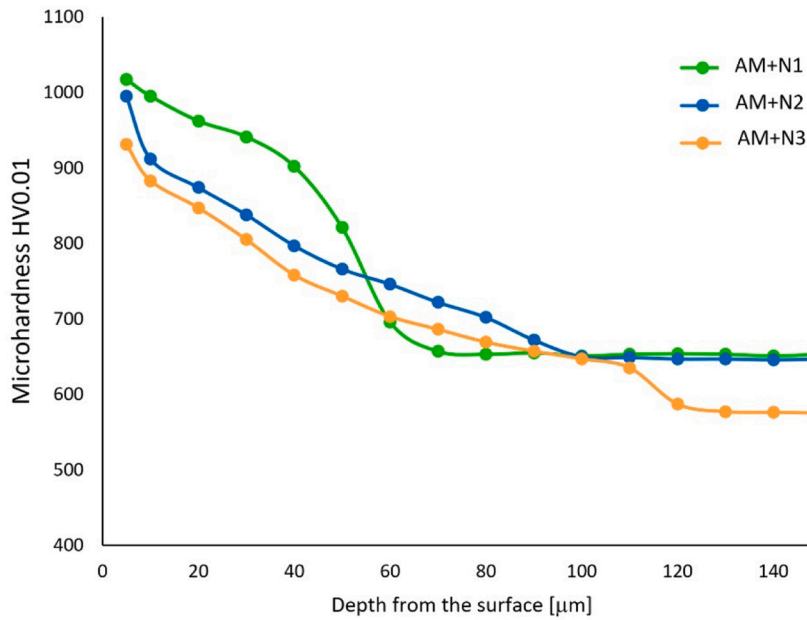

Fig. 8. Microhardness HV0.01 depth profile for nitride samples (AM+N1, AM+N2 and AM+N3).

The hardness profile of sample AM+N3 has, in the most part, the lowest values. The explanation of such strange hardness behaviour lies in the formation of the reverted austenite during nitriding. Higher nitriding temperatures favour the austenite content, and at the same time N penetration at the surface stabilizes the austenite.

Wear test results in the form of wear rate, calculated as the ratio between wear volume in mm³ and the product of the normal force and the total sliding distance in Nm are shown in Fig. 9a, and the coefficient of friction during the first 50 s (initial) and the average value for the steady-state conditions in Fig. 9b. For all the tested samples, regardless of the nitriding temperature used, abrasive wear was the dominant wear mechanism (Fig. 10), also resulting in the same steady-state friction of 0.72. However, the initial friction during the first 50 s of sliding does depend on the nitriding temperature. The highest nitriding temperature
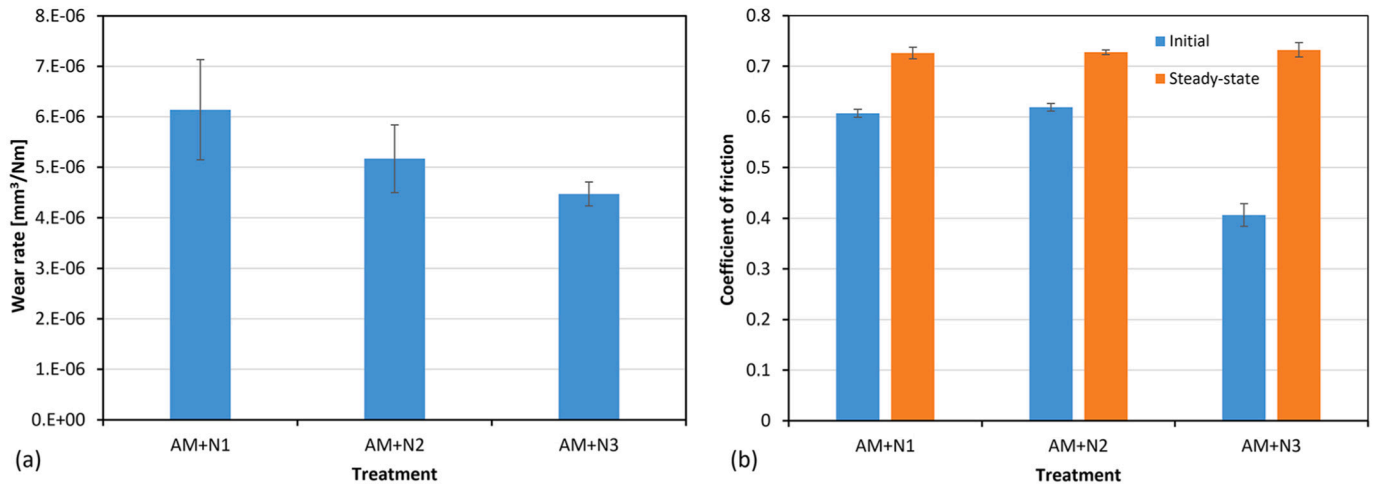
Fig. 9. (a) Wear rate and (b) coefficient of friction of samples AM+N1, AM+N2 and AM+N3.
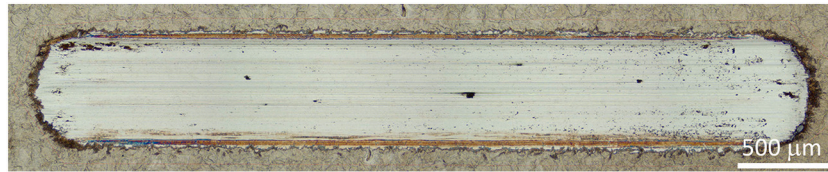

Fig. 10. Typical scar from abrasive wear (AM+N2).

of 520 °C (AM+N3) results in a lower initial coefficient of friction of ~0.4 (starting at 0.15 and increasing to 0.65 in the first 40–45 s), which then increases to 0.6 (starting at 0.45 and increasing to 0.65 in the first 10–20 s) as the nitriding temperature drops below 500 °C (AM+N1 & AM+N2, Fig. 9b and Fig. 11). The best wear resistance and wear rate of 4.5×10^{-6} mm^3/Nm is shown by the AM+N3 specimens, nitrided at the highest temperature of 520 °C. Reducing the nitriding temperature leads to higher wear. The wear rate for specimens AM+N2 (480 °C) increased to 5.1×10^{-6} mm^3/Nm and for specimens AM+N1, nitrided at the lowest temperature of 440 °C up to 6.1×10^{-6} mm^3/Nm. Although without a statistically significant difference, as determined by one-way ANOVA [40] ($F(2,6) = 4.260$, $p = 0.07$), wear test results do show decreasing wear rate trend with increased nitriding temperature

(Fig. 9a). In the current case the prevailing wear mechanism was abrasive wear, where the surface resistance to scratching and ploughing, provided by the hard surface layers, i.e., the compound layer, plays the dominant role. On the other hand, the presence of micro-cracks is not detrimental or crucial in such cases. The thick, hard compound layer, obtained at the highest nitriding temperature (AM+N3), thus provides the best wear resistance as well as a low initial friction, although some drop in the core hardness might take place. As long as the compound layer is thick enough to carry the load, the substrate/core hardness has only a negligible effect on wear resistance. However, as the compound-layer thickness is reduced (AM+N2) and becomes worn out or even absent (AM+N1), wear takes place within the diffusion zone. In this case the hardness depth distribution becomes important, with higher
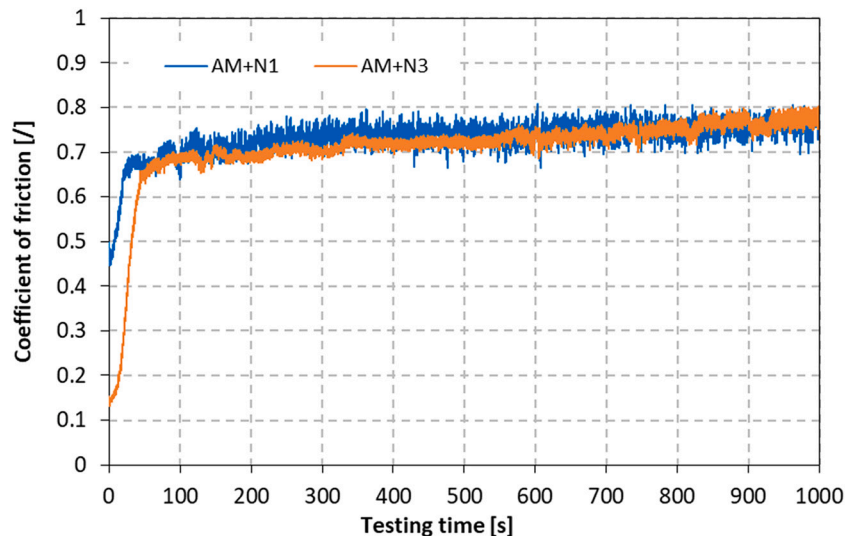

Fig. 11. Typical coefficient of friction curves for AM+N1 and AM+N3 samples.

material core hardness in general resulting in better abrasive-wear resistance. In the current case, the wear depth for the samples nitrided at the highest nitriding temperature (AM+N3) was within the compound layer zone (< 5 μm), and extended inside the bulk material (diffusion zone) for the specimens nitrided at lower temperatures, i.e., to 7.5 μm for AM+N2 and over 10 μm for AM+N1. Compound layer and diffusion zone thickness for the three nitriding temperatures (AM+N1, AM+N2 and AM+N3) were < 1 μm and ~ 55 μm, ~2 μm and ~ 90 μm, and ~ 5 μm and ~ 125 μm, respectively.

Our previous findings [26] show the beneficial role of heat treatment prior to nitriding in terms of a slightly better wear resistance and avoiding crack formation in compound layer. However, the present study shows that cracks can be avoided by nitriding at lower temperatures, but at the expense of diminishing wear resistance. On the other hand, for AM material a heat treatment before any surface thermochemical treatments is almost always valuable due to internal stress release and to homogenise the microstructure. The AM process with rapid solidification in most cases leads to nano/micro segregations and sometimes segregations along grain boundaries, which can contribute to new phase formations and in specific cases to the formation of cracks.

3.3. Corrosion properties

The corrosion performance of plasma-nitrided as built PBF-18Ni300 steel with respect to nitriding temperature was evaluated by using potentiodynamic measurements and the results are presented in Fig. 12. The electrochemical parameters defined from the potentiodynamic curves, i.e., the corrosion potential – E_{corr}, corrosion current density – i_{corr} and corrosion rate – v_{corr}, are listed in Table 2. The i_{corr} and the v_{corr} were calculated according to ASTM G102 – 89 (2015) [41]. Maraging steels are subjected to general corrosion predominantly due to the martensitic microstructure with Fe_2Mo and $Ni_3(Ti, Mo)$ precipitates [42]. As was already shown in our previous study, the nitriding considerably improved the corrosion resistance due to the formation of corrosion-resistant compound layer [26,43]. The potentiodynamic curves of the nitrided samples also revealed a passive region, which was not observed for the samples prior to the nitriding [26]. The AM+A3 sample exhibited a slightly broader passivation range with a breakdown potential (E_b) at approximately 100 mV(SCE), although shifted to higher corrosion-current densities, compared to E_b of around 0 mV(SCE) for the

other two samples, AM+N1 and AM+N2. At higher nitriding temperatures, a larger amount of austenite as well as a thicker nitride layer were determined. The interface between the austenite and the martensite enabled pitting corrosion. Furthermore, the cracks along the grain boundaries were observed in AM+A3 sample, which probably significantly influenced the corrosion process, leading to the shift of potentiodynamic curve to higher corrosion-current densities and increased corrosion rate.

4. Conclusions

In this investigation plasma nitriding was used to enhance the surface properties of 18Ni300 maraging steel produced by powder bed fusion. The nitriding temperature was varied to find the correlation between the nitriding temperature and the surface properties as well as microstructure evolution. The following conclusions can be drawn:

- The nitriding temperature influences the amount of retained/reverted austenite and at the same time causes Fe_2Mo and $Ni_3(Ti, Mo)$ precipitates to form. A higher nitriding temperature leads to a larger amount of austenite, which correlates with the Thermocalc simulation at equilibrium for certain temperatures.
- In the plasma nitride's compound layer, no precipitation was detected. The retained austenite transforms during nitriding mostly to Fe_4N and a small amount of TiN, while Ni diffuses to the phase borders. At the same time the martensite becomes rich in N and transforms to Fe_4N. A typical lamellar structure is observed, with segregation of the N and Co. The majority of the surface layer consists of Fe_4N with some martensite and austenite phases rich in N.
- A higher nitriding temperature leads to a thicker compound layer, but also to the formation of cracks, mostly occurring at different grain boundaries. The origin of the cracks is the internal stresses due
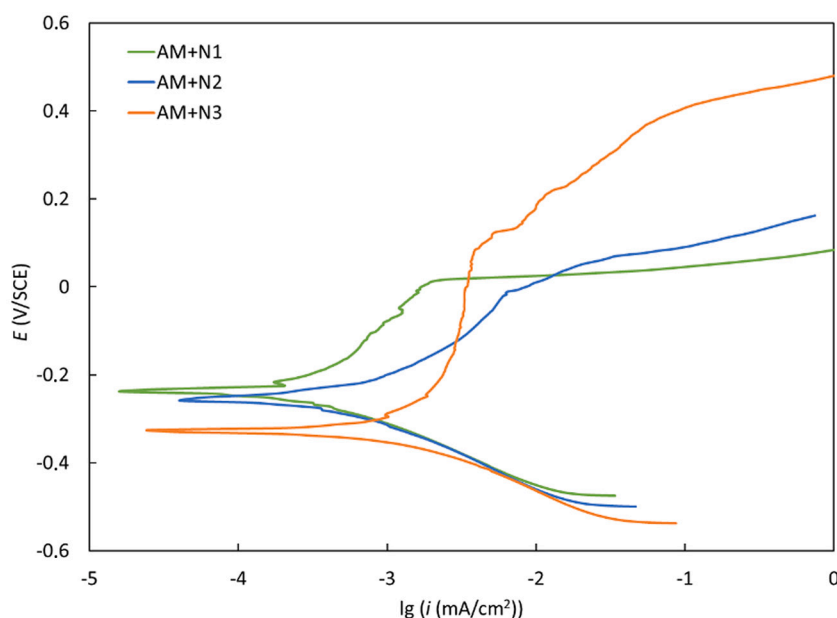
Table 2
Electrochemical parameters determined from the potentiodynamic curves.

Material	E_{corr} (mV)	i_{corr} (uA/cm^2)	v_{corr} (um/year)
AM+N1	−230 ± 2	0.30 ± 0.02	3.5 ± 0.1
AM+N2	−264 ± 2	0.56 ± 0.04	6.4 ± 0.2
AM+N3	−314 ± 3	0.88 ± 0.05	10.0 ± 0.2

Fig. 12. Potentiodynamic curves for maraging steel AM in 3.5% NaCl after plasma nitriding at three nitriding temperatures: N1 = 440 °C, N2 = 480 °C and N3 = 520 °C for 6 h.

to the additive manufacturing process, enhanced by the formation of an iron nitride phase along the grain boundaries. During PBF, segregation along the boundaries is observed with such a chemical composition, which leads to austenite phase formation. In the austenite phase area, the iron nitride is formed preferentially and causes a volume expansion.

- The sliding wear resistance with the dominated two-body abrasive wear mechanism increases with higher nitriding temperature where thicker compound layer is formed. Although surface cracks may be present, they do not have negative effect on sliding wear resistance. However, as the compound layer is worn out core hardness becomes the dominant factor in wear resistance of the nitrided surface.
- In general, plasma nitriding enhances the corrosion resistance. Small cracks developing at higher nitriding temperatures have significant role in corrosion properties.
- Based on the results, it can be concluded that a lower nitriding temperature is beneficial to avoid cracks, and at the same time the amount of austenite can be reduced. Depending on the specific applications, the nitriding time should be prolonged to obtain thicker compound layer and achieve optimal combination of surface properties.

CRediT authorship contribution statement

M. Godec: Conceptualization, Investigation, Supervision, Writing - original draft. F. Ruiz-Zepeda: Investigation. B. Podgornik: Investigation, Writing – review & editing. Č. Donik: Investigation. A. Kocijan: Investigation, Writing – review & editing. D.A. Skobir Balantič: Investigation, Writing – original draft.

Declaration of competing interest

None.

References

[1] W. Sha, Z. Guo, Maraging Steels: Modelling of Microstructure, Properties and Applications, Woodhead Publishing Limited, 2009, https://doi.org/10.1533/9781845696931.

[2] O. Moshka, M. Pinkas, E. Brosh, V. Ezersky, L. Meshi, Addressing the issue of precipitates in maraging steels - unambiguous answer, Mater. Sci. Eng., A 638 (2015) 232–239, https://doi.org/10.1016/j.msea.2015.04.067.

[3] F. Zhu, Y.F. Yin, R.G. Faulkner, Microstructural control of maraging steel C300, Mater. Sci. Technol. 27 (2011) 395–405, https://doi.org/10.1179/026708309X12506933873503.

[4] J. Mutua, S. Nakata, T. Onda, Z.-C. Chen, Optimization of selective laser melting parameters and influence of post heat treatment on microstructure and mechanical properties of maraging steel, Mater. Des. 139 (2018) 486–497, https://doi.org/10.1016/j.matdes.2017.11.042.

[5] B.-Z. Weiss, Maraging steels—structure, properties and applications, in: N.R. Comins, J.B. Clark (Eds.), Spec. Steels Hard Mater, Elsevier, 1983, pp. 35–54, https://doi.org/10.1016/B978-0-08-029358-5.50009-4.

[6] F.F. Conde, J.D. Escobar, J.P. Oliveira, A.L. Jardini, W.W. Bose Filho, J.A. Avila, Austenite reversion kinetics and stability during tempering of an additively manufactured maraging 300 steel, Addit. Manuf. 29 (2019), 100804, https://doi.org/10.1016/j.addma.2019.100804.

[7] M.N. Rao, Progress in understanding the metallurgy of 18 \% nickel maraging steels, Int. J. Mater. Res. 97 (2006) 1594–1607, https://doi.org/10.3139/146.101418.

[8] E.A. Jaegle, P.-P. Choi, J. Van Humbeeck, D. Raabe, Precipitation and austenite reversion behavior of a maraging steel produced by selective laser melting, J. Mater. Res. 29 (2014) 2072–2079, https://doi.org/10.1557/jmr.2014.204.

[9] M. Farooque, H. Ayub, A.U. Haq, A.O. Khan, The formation of reverted austenite in 18\% ni 350 grade maraging steel, J. Mater. Sci. 33 (1998) 2927–2930, https://doi.org/10.1023/A:1004346412079.

[10] M.F. Yan, Y.Q. Wu, R.L. Liu, M. Yang, L.N. Tang, Microstructure and mechanical properties of the modified layer obtained by low temperature plasma nitriding of nanocrystallized 18Ni maraging steel, Mater. Des. 47 (2013) 575–580, https://doi.org/10.1016/j.matdes.2012.11.007.

[11] J. Fernández de Ara, E. Almandoz, J.F. Palacio, G.G. Fuentes, Simultaneous ageing and plasma nitriding of grade 300 maraging steel: how working pressure determines the effective nitrogen diffusion into narrow cavities, Surf. Coat. Technol. 317 (2017) 64–74, https://doi.org/10.1016/j.surfcoat.2017.02.060.

[12] Y. Hong, D.D. Dong, S.S. Lin, W. Wang, C.M. Tang, T.C. Kuang, M.J. Dai, Improving surface mechanical properties of the selective laser melted 18Ni300 maraging steel via plasma nitriding, Surf. Coat. Technol. 406 (2021), 126675, https://doi.org/10.1016/j.surfcoat.2020.126675.

[13] J. Fernández de Ara, E. Almandoz, J.F. Palacio, G.G. Fuentes, R.J. Rodríguez, J.A. García, Influence of temperature in arc-activated plasma nitriding of maraging steel in solution annealed and aged conditions, Surf. Coat. Technol. 258 (2014) 754–762, https://doi.org/10.1016/j.surfcoat.2014.07.084.

[14] A.G. dos Reis, D.A.Pereira Reis, A.J. Abdalla, J. Otubo, S. Zepka, A.A. Couto, V.H. Baggio Scheid, Effect of simultaneous plasma nitriding and aging treatment on the microstructure and hardness of maraging 300 steel, in: A. Ochsner, H. Altenbach (Eds.), Mech. Mater. Eng. Mod. Struct. Compon. Des., 2015, pp. 277–284, https://doi.org/10.1007/978-3-319-19443-1_22.

[15] J. Suryawanshi, K.G. Prashanth, U. Ramamurty, Tensile, fracture, and fatigue crack growth properties of a 3D printed maraging steel through selective laser melting, J. Alloys Compd. 725 (2017) 355–364, https://doi.org/10.1016/j.jallcom.2017.07.177.

[16] C. Tan, K. Zhou, W. Ma, P. Zhang, M. Liu, T. Kuang, Microstructural evolution, nanoprecipitation behavior and mechanical properties of selective laser melted high-performance grade 300 maraging steel, Mater. Des. 134 (2017) 23–34, https://doi.org/10.1016/j.matdes.2017.08.026.

[17] R. Branco, J. Silva, J.M. Ferreira, J.D. Costa, C. Capela, F. Berto, L. Santos, F.V. Antunes, Fatigue behaviour of maraging steel samples produced by SLM under constant and variable amplitude loading, Procedia Struct. Integr. 22 (2019) 10–16, https://doi.org/10.1016/j.prostr.2020.01.002.

[18] E.A. Jaegle, Z. Sheng, P. Kuernsteiner, S. Ocylok, A. Weisheit, D. Raabe, Comparison of maraging steel micro- and nanostructure produced conventionally and by laser additive manufacturing, Materials (Basel) 10 (2017), https://doi.org/10.3390/ma10010008.

[19] Y. Bai, D. Wang, Y. Yang, H. Wang, Effect of heat treatment on the microstructure and mechanical properties of maraging steel by selective laser melting, Mater. Sci. Eng. A 760 (2019) 105–117, https://doi.org/10.1016/j.msea.2019.05.115.

[20] R. Casati, J. Lemke, A. Tuissi, M. Vedani, Aging behaviour and mechanical performance of 18-ni 300 steel processed by selective laser melting, Metals (Basel) 6 (2016) 218, https://doi.org/10.3390/met6090218.

[21] K. Monkova, I. Zetkova, L. Kučerová, M. Zetek, P. Monka, M. Daňa, Study of 3D printing direction and effects of heat treatment on mechanical properties of MS1 maraging steel, Arch. Appl. Mech. 89 (2019) 791–804, https://doi.org/10.1007/s00419-018-1389-3.

[22] B. Mooney, K.I. Kourousis, R. Raghavendra, Plastic anisotropy of additively manufactured maraging steel: influence of the build orientation and heat treatments, Addit. Manuf. 25 (2019) 19–31, https://doi.org/10.1016/j.addma.2018.10.032.

[23] C. Tan, K. Zhou, M. Kuang, W. Ma, T. Kuang, Microstructural characterization and properties of selective laser melted maraging steel with different build directions, Sci. Technol. Adv. Mater. 19 (2018) 746–758, https://doi.org/10.1080/14686996.2018.1527645.

[24] S. Yin, C. Chen, X. Yan, X. Feng, R. Jenkins, P. O'Reilly, M. Liu, H. Li, R. Lupoi, The influence of aging temperature and aging time on the mechanical and tribological properties of selective laser melted maraging 18Ni-300 steel, Addit. Manuf. 22 (2018) 592–600, https://doi.org/10.1016/j.addma.2018.06.005.

[25] M. Godec, C. Donik, A. Kocijan, B. Podgornik, D.A.S. Balantic, Effect of post-treated low-temperature plasma nitriding on the wear and corrosion resistance of 316L stainless steel manufactured by laser powder-bed fusion, Addit. Manuf. 32 (2020), https://doi.org/10.1016/j.addma.2019.101000.

[26] M. Godec, B. Podgornik, A. Kocijan, Č. Donik, D.A.S. Balantič, Use of plasma nitriding to improve the wear and corrosion resistance of 18Ni-300 maraging steel manufactured by selective laser melting, Sci. Rep. 11 (2021) 3277, https://doi.org/10.1038/s41598-021-82572-y.

[27] U.K. Viswanathan, G.K. Dey, M.K. Asundi, Precipitation hardening in 350 grade maraging steel, Metall. Trans. A. 24 (1993) 2429–2442, https://doi.org/10.1007/BF02646522.

[28] V.K. Vasudevan, S.J. Kim, C.M. Wayman, Precipitation reactions and strengthening behavior in 18 wt pct nickel maraging steels, Metall. Trans. A. 21 (1990) 2655–2668, https://doi.org/10.1007/BF02646061.

[29] R. Casati, J.N. Lemke, A. Tuissi, M. Vedani, Aging behaviour and mechanical performance of 18-ni 300 steel processed by selective laser melting, Metals (Basel) 6 (2016), https://doi.org/10.3390/met6090218.

[30] E.A. Jägle, Z. Sheng, L. Wu, L. Lu, J. Risse, A. Weisheit, D. Raabe, Precipitation reactions in age-hardenable alloys during laser additive manufacturing, JOM 68 (2016) 943–949, https://doi.org/10.1007/s11837-015-1764-2.

[31] N. Haghdadi, M. Laleh, M. Moyle, S. Primig, Additive manufacturing of steels: a review of achievements and challenges, J. Mater. Sci. 56 (2021) 64–107, https://doi.org/10.1007/s10853-020-05109-0.

[32] M. Godec, S. Zaefferer, B. Podgornik, M. Šinko, E. Tchernychova, Quantitative multiscale correlative microstructure analysis of additive manufacturing of stainless steel 316L processed by selective laser melting, Mater. Charact. 160 (2020), 110074, https://doi.org/10.1016/j.matchar.2019.110074.

[33] Y.M. Wang, T. Voisin, J.T. McKeown, J. Ye, N.P. Calta, Z. Li, Z. Zeng, Y. Zhang, W. Chen, T.T. Roehling, R.T. Ott, M.K. Santala, P.J. Depond, M.J. Matthews, A. V. Hamza, T. Zhu, Additively manufactured hierarchical stainless steels with high strength and ductility, Nat. Mater. 17 (2018) 63–71, https://doi.org/10.1038/nmat5021.

[34] R. Acevedo, P. Sedlak, R. Kolman, M. Fredel, Residual stress analysis of additive manufacturing of metallic parts using ultrasonic waves: state of the art review, J. Mater. Res. Technol. 9 (2020) 9457–9477, https://doi.org/10.1016/j.jmrt.2020.05.092.

[35] C. Li, Z.Y. Liu, X.Y. Fang, Y.B. Guo, Residual stress in metal additive manufacturing, Procedia CIRP. 71 (2018) 348–353, https://doi.org/10.1016/j.procir.2018.05.039.

[36] M.A. Peck, M.A. Langell, Comparison of nanoscaled and bulk NiO structural and environmental characteristics by XRD, XAFS, and XPS, Chem. Mater. 24 (2012) 4483–4490, https://doi.org/10.1021/cm300739y.

[37] K. Nakata, W. Yamauchi, K. Akamatsu, M. Ushio, Plasma nitriding behavior of low carbon binary alloy steels, Surf. Coat. Technol. 174 (2003) 1206–1210, https://doi.org/10.1016/S0257-8972(03)00459-6.

[38] Č. Donik, J. Kraner, I. Paulin, M. Godec, Influence of the energy density for selective laser melting on the microstructure and mechanical properties of stainless steel, Metals (Basel) 10 (2020), https://doi.org/10.3390/met10070919.

[39] V. Alexis, R. Frédéric, Q. Jean, A. Eric, Determination of gray cast iron age strengthening by nondestructive methods: effect of alloying elements, J. Mater. Eng. Perform. 28 (2019) 4026–4033, https://doi.org/10.1007/s11665-019-04180-2.

[40] H.J. Seltman, in: Experimental Design and Analysis, Chapter 7: One-way ANOVA, Carnegie Mellon University, 2018, pp. 171–190.

[41] ASTM G102-89(2015)e1, Standard Practice for Calculation of Corrosion Rates and Related Information from Electrochemical Measurements, 2015.

[42] C. Tan, K. Zhou, M. Kuang, W. Ma, T. Kuang, Microstructural characterization and properties of selective laser melted maraging steel with different build directions, Sci. Technol. Adv. Mater. 19 (1) (2018) 746–758, https://doi.org/10.1080/14686996.2018.1527645.

[43] N. Kumar, S. Sharma, B. Ganguli, Enhancement of surface properties of maraging steel C300 by plasma nitriding, Int. J. Eng. Res. Technol. 4 (2018).